Supplementary Information (SI) for Energy & Environmental Science.

Supporting Information

Chlorinated Polypropylene Enables Stress-Dissipative Networks and High Efficiency in Intrinsically Stretchable Organic Photovoltaics

Shuiwang Lv, Huizhen Ke, Yuting Wang, Dexia Han, Bei Li, Vakhobjon Kuvondikov, Wenchao Zhao*, Menglan Lv*, Long Ye**

S. Lv, H. Ke

School of Textiles and Clothing, Xinjiang University, Xinjiang, China.

S. Lv, H. Ke

Fujian Key Laboratory of Functional Textile Fibers and Products, Faculty of Clothing and Design, Minjiang University, Fuzhou 350108, China.

Email: kehuizhen2018@mju.edu.cn

Y. Wang, W. Zhao

Co-Innovation Center of Efficient Processing and Utilization of Forest Resources College of Materials Science and Engineering Nanjing Forestry University, Nanjing, China.

Email: wenchaozhao@njfu.edu.cn

S. Lv, D. Han, B. Li, L. Ye

School of Materials Science and Engineering, State key Laboratory of Advanced Materials for Intelligent Sensing, Tianjin Key Laboratory of Molecular Optoelectronic Sciences, Key Laboratory of Organic Integrated Circuits, Ministry of Education, Collaborative Innovation Center of Chemical Science and Engineering (Tianjin), Tianjin University, Tianjin, China.

Email: yelong@tju.edu.cn

V. Kuvondikov

Institute of Ion-Plasma and Laser Technologies, Uzbekistan Academy of Sciences, 33, Durmon yuli, Tashkent, Uzbekistan.

M. Lv

Engineering Research Center for Energy Conversion and Storage Technology of Guizhou, School of Chemistry and Chemical Engineering, Guizhou University, Guiyang, China.

Email: mllv@gzu.edu.cn

Experimental Section/Methods

Materials: All reagents for photoactive films were sourced from Solarmer Materials Inc. Poly(3,4-ethylenedioxythiophene):Poly(styrenesulfonate) (PEDOT:PSS, grade Baytron PVP A14083) and PDINN were obtained from Clevios™ and Derthon Optoelectronic Materials Science Technology Co., Ltd., individually. All organic solvents were acquired from Sigma-Aldrich or Heowns, and employed as received without additional purification. PP-Cl was procured from Kmart Co., Ltd. The chlorinated polypropylene (PP-Cl) used in this work was purchased from RHAWN Reagent with catalog number R139417, CAS number 68442-33-1, and analytical grade (AR). The certificate of analysis (COA) for the specific batch used (lot number RH841204) indicates a purity of 98.28%, a solid appearance, a chlorine content of 32 ± 1 wt%, and the Molecular weight of 146 k.

Rigid organic solar cells fabrication and characterization: The devices were fabricated with a conventional structure of ITO/2PACz/Active layer/PDINN/Ag.[1-10] All solution-based fabrication processes were carried out in a argon-filled glove box, except for initial material weighing.

Binary devices (PM6:BTP-eC9):PM6 and BTP-eC9 were co-dissolved in chloroform at a 1:1.2 mass ratio, with PM6 concentration fixed at 7 mg/mL. PP-Cl stock solution (10 mg/mL in chloroform) was added at different mass ratios, and the mixture was stirred at 60 °C for 2 h. Pre-cleaned ITO substrates were UV-ozone treated before transfer to the glove box. The 2PACz hole transport layer (0.3 mg/mL in methanol) was spin-coated at 5000 rpm and annealed at 100 °C for 10 min. The active layer was deposited at 2000 rpm for 40 s, followed by annealing at 100 °C for 5 min to form a ~110 nm thin film. PDINN was dissolved in methanol to prepare a 1 mg/mL stock solution, which was centrifuged at 3000 rpm for 30 seconds prior to spin-coating as the electron transport layer. Finally, a 150 nm thick silver electrode was thermally evaporated under a high vacuum of 5×10^{-5} Pa.

Ternary devices (D18:BTP-eC9:L8-BO): The active layer precursor was prepared by co-dissolving D18, BTP-eC9 and L8-BO in chloroform at a 1:1.1:0.2 mass ratio (D18, 5 mg/mL), with 5 wt% PP-Cl added. The solution was stirred at 60 °C for 2 h, then spin-coated at 3000 rpm and annealed at 80 °C for 5 min (~110 nm). The deposition of 2PACz, PDINN and silver electrode was identical to that of the binary devices.

Intrincially stretchable organic solar cells fabrication: The devices were fabricated with a conventional structure of TPU/ PH1000/PEDOT:PSS/Active layer/PDINN/EGaIn. The fabrication and spin-coating conditions for the active layer remained consistent with those adopted for the aforementioned rigid devices. The fabrication processes, spin-coating conditions and annealing temperatures for the remaining functional layers were carried out in accordance with prior literature.[11-18]

Photovoltaic device characterization: Current density-voltage (*J*-*V*) profiles of the fabricated devices were recorded using a Keithley 2400 source meter coupled with an AAA solar simulator (model SS-F5-3A, Enli Technology Co., Ltd., Taiwan), under AM 1.5G irradiation at an intensity of 100 mA cm^{-2}. All testing procedures were conducted in a nitrogen-filled environment. External quantum efficiency (EQE) spectra were acquired via the Solar Cell Spectral Response Measurement System QE-R3011 (Enli Technology Co., Ltd., Taiwan). The thickness of the blend films was determined with a Bruker Dektak XT surface profilometer. During the photovoltaic characterization of stretchable devices, the Poisson's ratio of the TPU substrate was set to 0.415 following the well-established protocol reported by Li *et al.*[19], which was used to correct the effective illuminated area of the devices under different tensile strains and ensure the accuracy of short-circuit current density (J_{sc}) calculations.

***Microstructure Measurements*:** GIWAXS characterization was implemented at the BL02U2 beamline of the Beijing Synchrotron Radiation Facility (BSRF). Monochromatic X-rays at 10.5 keV, with a corresponding wave length of 1.31 Å, served as the probing source. A grazing incidence angle was tuned to 0.17°, while the separation between test specimens and the signal recorder was fixed at 175 mm. Lanthanum hexaboride standard samples were adopted to correct the central ray position and detector spacing. Thin-film specimens were fabricated via solution spin-casting on silicon substrates, maintaining the same processing parameters as those for photovoltaic units. Specialized GIWAXS-Tools software was applied to process raw signals, eliminate background interference from silicon substrates, and unify all testing outcomes..

The film’s surface morphology was examined with atomic force microscopy (AFM) (Bruker Multimode 8) in tapping mode at a scanning speed of 1 Hz and a range of 2 μm × 2 μm. The AFM cantilever used was RTESPA-300, with a spring constant of approximately 40 N/m.

Transmission electron microscopy (TEM) images were obtained using a JEOL JEM-2100PLUS microscope. The film was prepared under the same conditions as for the device. After dissolving the sacrificial layer, the film floated on water, was transferred to a copper grid, and placed in a vacuum overnight to remove moisture.

***Mechanical Measurements*:** The thin-film stress-strain curves were obtained using a commercial instrument (designed by Yangzhou Super-Flex-Tech Company, No. ZRA-01, China). In the process of collecting data, the FAST measurement technique was utilized.The experimental procedures and testing protocols for FAST characterization were fully implemented in strict accordance with the previous study reported by Feng et al.[20]

Prediction of modulus of blend films: All elastic modulus predictions and fittings based on the Coran-Patel model for the blend films were carried out in strict accordance with the standardized procedures detailed in the previous works by Peng et al.[21] and Sun et al.[22, 23]. In the Coran-Patel model, E_u and E_l denote the upper and lower theoretical bounds of the composite modulus, derived from the classical Voigt and Reuss mixing rules, respectively, and are expressed as:

$$E_u = E_h \phi_h + E_s \phi_s$$

$$E_l = \frac{E_s E_h}{\phi_h E_s + \phi_s E_h}$$

where E_h corresponds to the elastic modulus of the neat hard conjugated polymer phase (PM6:BTP-eC9), and E_s corresponds to that of the neat soft elastomer phase (PP-Cl).

Supplementary figures & tables

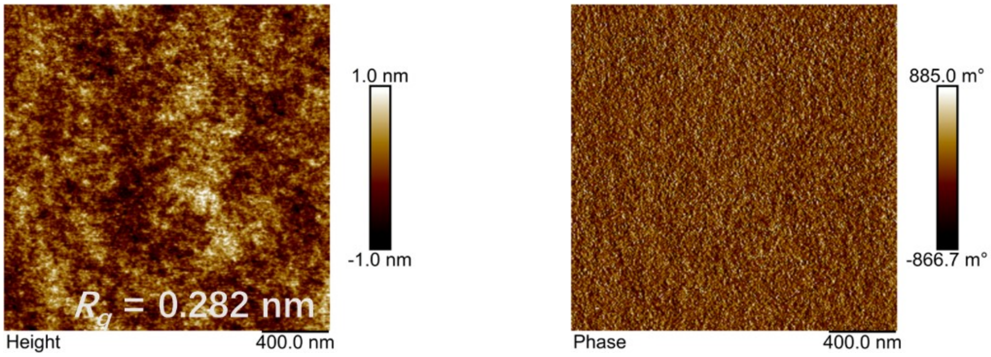

Figure S1. The AFM height image, phase image and Root-mean-square roughness (R_q) of pure PP-Cl.

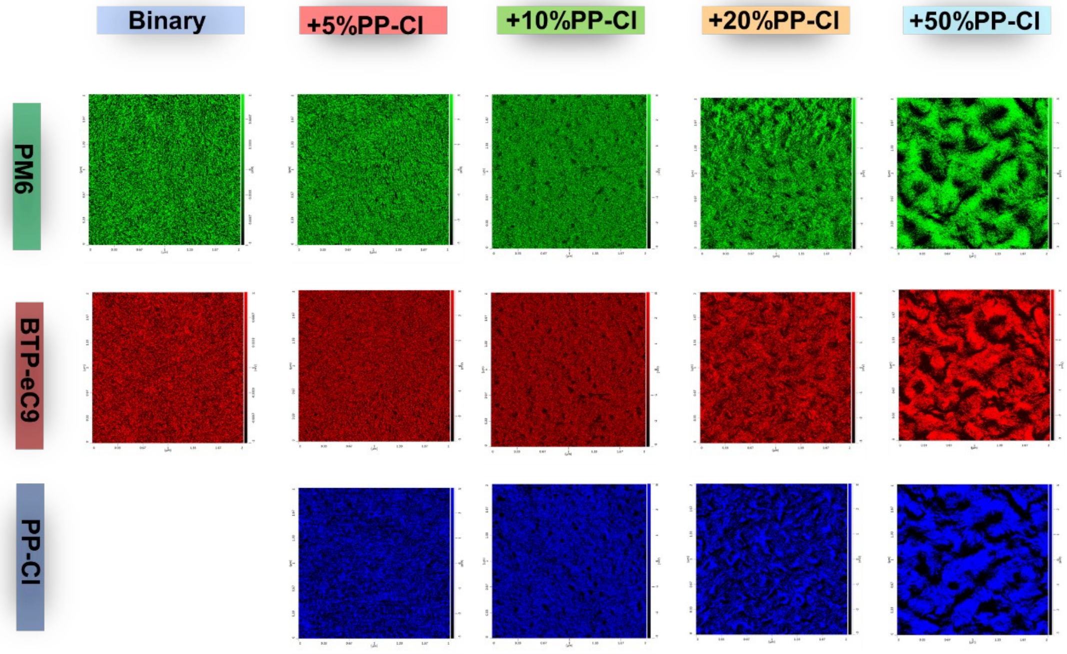

Figure S2. 2D Fluorescence resonance energy transfer (FRET) characterization of IS-OPVs active layers with varying PP-Cl additive contents.

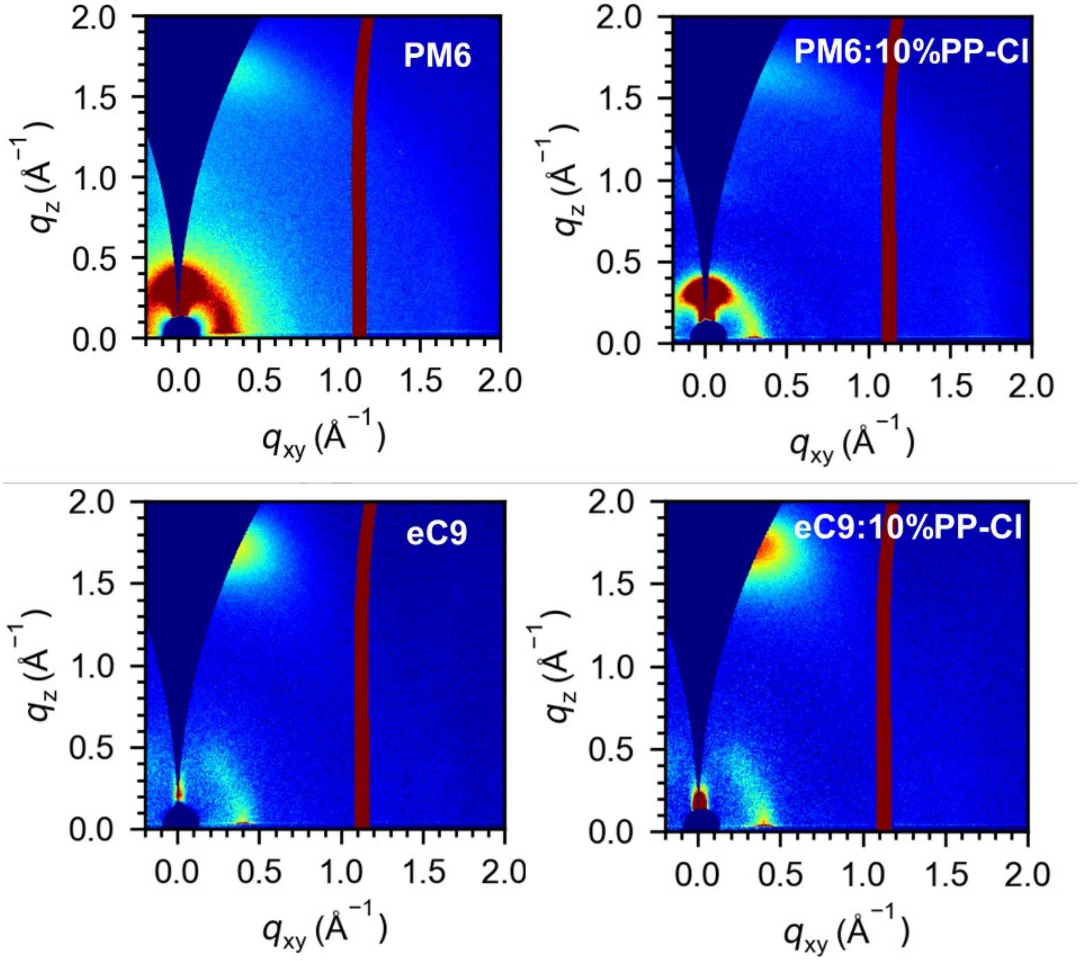

Figure S3. 2D GIWAXS pattern of a pristine PM6, PM6:10% PP-Cl, TP-eC9, BTP-eC9:10% PP-Cl films.

Table S1. The molecular stacking characteristics parameters of PM6, BTP-eC9, PP-Cl films, including peaks position (*q*), *d*-spacing, full width at half maximum (*FWHM*), coherence length (*CL*).

OOP of (100)

	q (Å^{-1})	*d*-spacing (Å)	*FWHM*(Å^{-1})	*CL* (Å)
PM6	0.31	20.26	0.168	33.64
BTP-eC9	0.31	20.26	0.407	13.88

OOP of (010)

	q (Å^{-1})	*d*-spacing (Å)	*FWHM*(Å^{-1})	*CL* (Å)
PM6	1.68	3.74	0.274	20.62
BTP-eC9	1.72	3.65	0.317	17.83

IP of (100)

	q (Å^{-1})	*d*-spacing (Å)	*FWHM*(Å^{-1})	*CL* (Å)
PM6	0.30	20.93	0.149	37.93
BTP-eC9	0.34	18.47	0.288	19.63
PP-Cl	0.33	19.03	0.315	17.94

Table S2. The molecular stacking characteristics parameters of blend films with different PP-Cl, including peaks position (*q*), d-spacing (*d*), full width at half maximum (*FWHM*). coherence length (*CL*).

OOP of (100)

Blend films	*q* (Å^{-1})	*d*-spacing (Å)	*FWHM* (Å^{-1})	*CL* (Å)
0% PP-Cl	0.259	24.2	0.169	33.44
5% PP-Cl	0.264	23.8	0.143	39.52
10% PP-Cl	0.277	22.7	0.185	30.55
20% PP-Cl	0.302	20.8	0.161	35.11
50% PP-Cl	0.311	20.2	0.139	40.66

OOP of (010)

Blend films	*q* (Å^{-1})	*d*-spacing (Å)	*FWHM* (Å^{-1})	*CL* (Å)
0% PP-Cl	1.70	3.6	0.293	19.29
5% PP-Cl	1.71	3.7	0.292	19.36
10% PP-Cl	1.71	3.8	0.291	19.42
20% PP-Cl	1.71	3.7	0.301	18.78
50% PP-Cl	1.72	3.7	0.261	21.66

IP of (100)

Blend films	q (Å^{-1})	d-spacing (Å)	$FWHM$ (Å^{-1})	CL (Å)
0% PP-Cl	0.32	19.0	0.185	30.55
5% PP-Cl	0.33	19.0	0.173	32.67
10% PP-Cl	0.32	19.0	0.228	24.79
20% PP-Cl	0.32	19.0	0.210	26.91
50% PP-Cl	0.32	19.6	0.244	23.16

Table S3. Key parameters of the PP-Cl active layer films with different mass fractions were obtained from Stress-Strain curves. According to experience, the elastic modulus is defined as the slope of the stress-strain curve measured by the FAST test within the first 3.8% strain [a].

Elastomer	Modulus (GPa)	Fracture Strain (%)	Stress (MPa)	Toughness (J/m^3)
0% PP-Cl	0.916±0.013	3.9±0.1	31.35±1.41	521.27±12.06
5% PP-Cl	0.642±0.009	5.3±0.3	34.27±2.96	778.61±19.25
10% PP-Cl	0.398±0.010	6.8±0.3	35.54±1.77	933.11±21.81
20% PP-Cl	0.262±0.005	8.7±0.2	35.62±2.04	1235.35±29.42
50% PP-Cl	0.182±0.003	14.8±0.5	35.31±2.39	2567.44±39.67
100% PP-Cl	0.092±0.0004	225.6±12.3	12.23±0.97	23034.1±145.39

[a] All the detailed data were obtained by averaging the data of the 6 samples.

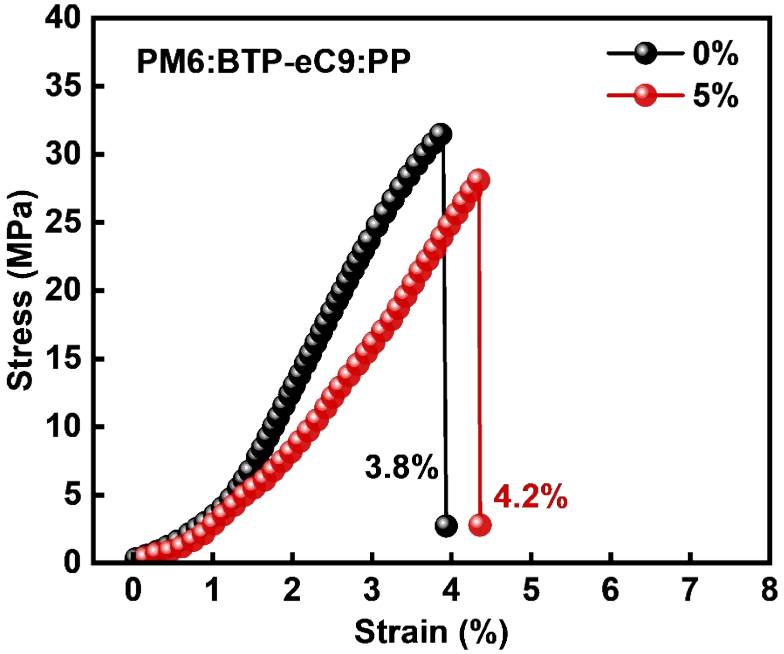

Figure S4 Stress-strain curves of the PM6:BTP-eC9 blend films with 5%wt PP contents.

Table S4. Crack onset strain of PM6:BTP-eC9:PP-Cl films with varying PP-Cl contents, obtained from the FOE test [a].

PP-Cl	**0%**	**5%**	**10%**	**20%**	**50%**
COS (%)	4.8±0.3	6.2±0.2	8.1±0.4	10.4±0.9	17.1±0.5

[a] All the detailed data were obtained by averaging the data of the 6 samples.

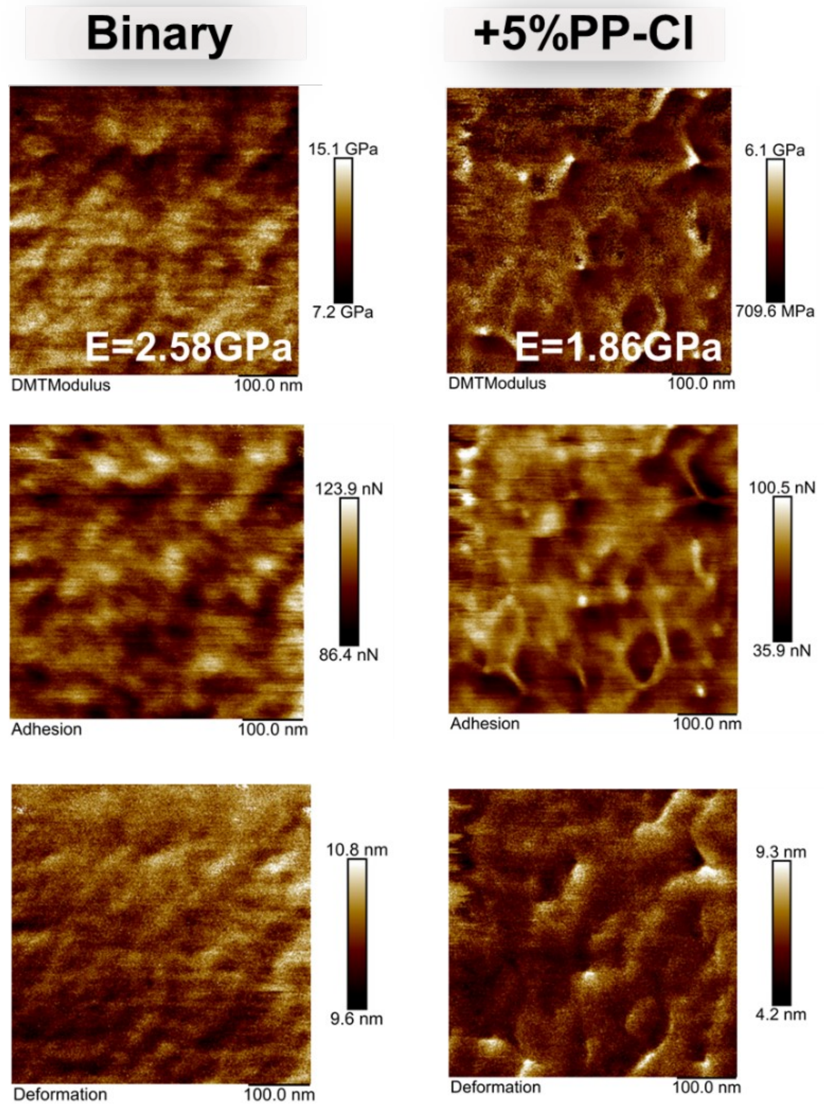

Figure S5. DMT modulus, adhesion, and deformation maps of PM6:BTP-eC9:PP-Cl blend films. The values shown in the DMT modulus images represent area-averaged elastic moduli. All images were acquired over a 2 ×2 μm scan area.

Table S5. Photovoltaic parameters of PM6:BTP-eC9:PP-Cl based *Rigid OPVs* [a].

Active layer	V_{OC}**(V)**	J_{SC} **(mA/cm^2)**	**FF (%)**	**PCE (%)**
PM6:BTP-eC9	0.851	28.13	75.38	18.04 (17.92±0.11)
+5%PP-Cl	0.850	27.79	79.16	18.69 (18.39±0.20)
+10%PP-Cl	0.855	27.42	78.92	18.50 (18.13±0.31)
+20%PP-Cl	0.855	26.51	75.82	17.18 (16.71±0.31)
+50%PP-Cl	0.849	23.85	68.20	13.80 (13.17±0.49)

[a] All the detailed PCE data were obtained by averaging the data of the 6 samples.

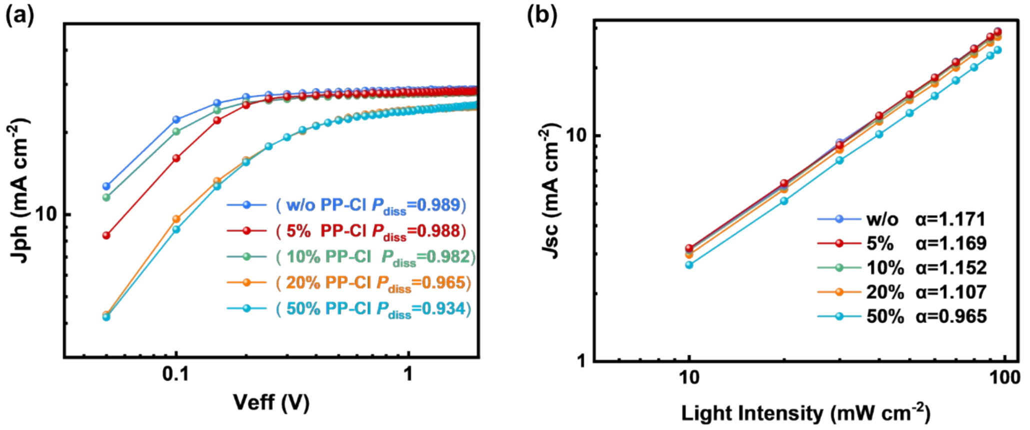

Figure S6. J_{ph}–V_{eff} characteristics of devices with different PP-Cl concentrations, showing a gradual decrease in exciton dissociation probability (P_{diss}) with increasing additive loading. (b) Light intensity dependence of J_{sc}, where the decreasing α indicates enhanced bimolecular recombination in high-PP-Cl devices.

Table S6. Photovoltaic performance of *IS-OPVs* under the optimized conditions [a)].

Active layer	V_{OC} (V)	J_{SC} (mA/cm^2)	FF (%)	PCE (%)
PM6:BTP-eC9	0.815	26.72	68.96	15.02 (14.88±0.11)
PM6:BTP-eC9:5%PP-Cl	0.818	26.53	71.53	15.54 (15.16±0.36)

[a)] All the detailed PCE data were obtained by averaging the data of the 6 samples.

Table S7. Under optimized conditions, the photovoltaic performance of an ultra-large-area device with an area of 100 cm², based on PM6:BTP-eC9:5% PP-Cl.

PCE (%)	V_{OC}(V)	J_{SC} (mA/cm2)	FF (%)	Rs
11.7 (11.3±0.15)	17.1 (17.0±0.08)	23.2 (23.1±0.05)	58.7 (56.8±0.64)	42.9 (42.1±0.64)

[a)] All the detailed data were obtained by averaging the data of the 6 samples.

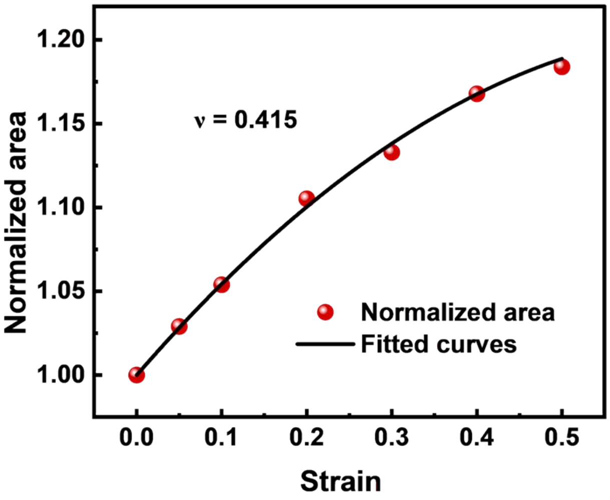

Figure S7 Fitting graph of the device area of IS-OPVs with Poisson's ratio $\nu = 0.415$.

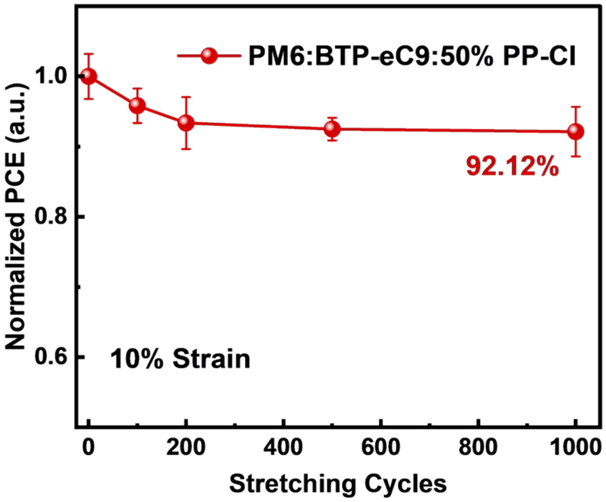

Figure S8**.** Normalized PCE of the devices of PM6:BTP-eC9:50%PP-Cl based *IS-OPVs* as a function of stretching cycles under 10% engineering strain.

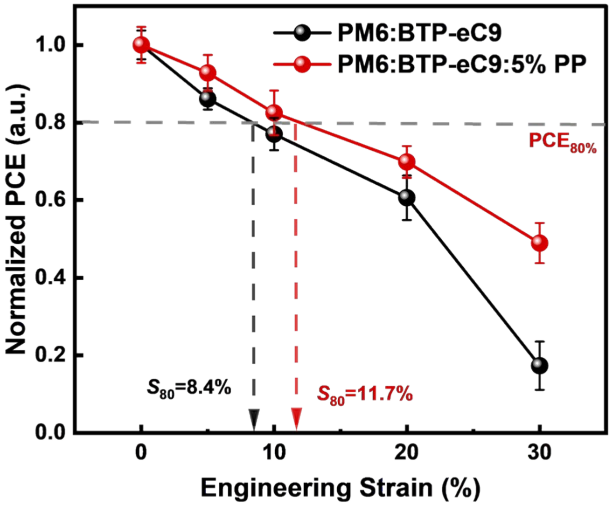

Figure S9**.** Normalized PCE of the devices of PM6:BTP-eC9:5%PP based *IS-OPVs*.

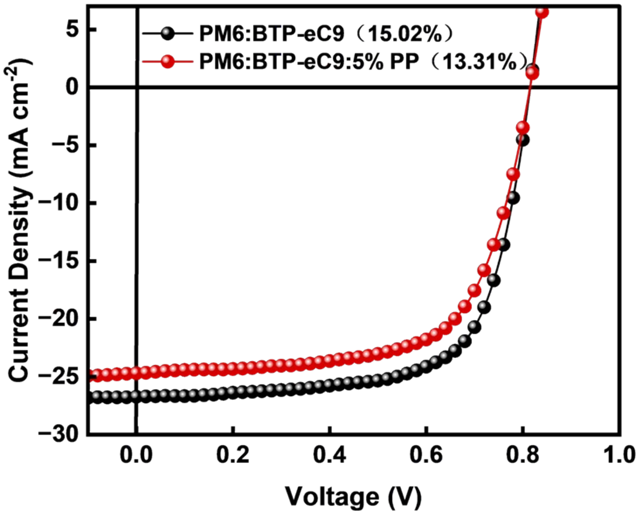

Figure S10**.** *J-V* curves of the PM6:BTP-eC9 stretchable devices with and without 5 wt% PP

Table S8. Photovoltaic performance of *IS-OPVs* under the optimized conditions [a)].

Active layer	**V_{OC} (V)**	**J_{SC} (mA/cm^2)**	**FF (%)**	**PCE (%)**
PM6:BTP-eC9	0.815	26.72	68.96	15.02 (14.88±0.11)
PM6:BTP-eC9:5%PP	0.814	24.69	66.15	13.31 (13.19±0.08)

a) All the detailed PCE data were obtained by averaging the data of the 6 samples.

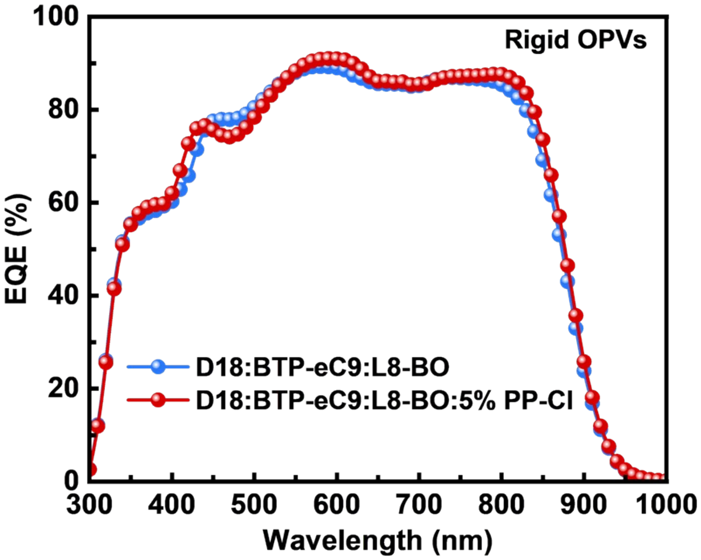

Figure S11. External quantum efficiency (EQE) spectra of rigid D18:BTP-eC9:L8-BO ternary organic solar cells with and without 5 wt% PP-Cl.

Table S9. Photovoltaic parameters of D18:BTP-eC9:L8-BO: 5% PP-Cl based *Rigid OPVs*.

Active layer	V_{OC}(V)	J_{SC} (mA/cm^2)	FF (%)	PCE (%)
D18:BTP-eC9:L8-BO	0.871	28.20	80.79	19.85 (19.44 ± 0.25)
D18:BTP-eC9:L8-BO:PP-Cl	0.870	28.72	82.04	20.50 (20.05 ± 0.25)

[a] All the detailed PCE data were obtained by averaging the data of the 6 samples.

Table S10. PCE_{max} and device structure of polymer donor:BTP-eC9-based *rigid OPVs* reported in the literature and in this work.

Device structure	**Active layer**	**PCE $_{max}$ (%)**	**Ref.**
ITO/PEDOT:PSS/Active layer/PDINN/Al	PM6: Y6-BO	15.7	[24]
	PM6-ThOH: Y6-BO	16.8	
	PM6-ThEG: Y6-BO	16.3	
	PM6-ThOH: PM6-ThEG: Y6-BO	17.4	
ITO/PEDOT:PSS / Active layer /NDI-Ph/Ag	D18:L8-BO	18.01	[25]
	PBQx-TF:BTP-eC9-2Cl	18.26	
ITO/PEDOT:PSS/Active layer/PDINO/Al	PM6:ID-C6Ph-ST-4F (1:1.25)	15.36	[10]
	PM6:ID-C6Ph-ST-4F (1:1.5)	13.65	
	PM6:ID-C6Ph-ST-4F (1:1)	13.50	
ITO/PEDOT:PSS /Active layer/ PDINN/Ag.	PM6:Y6-BO	15.83	[26]
	PM6-B10:Y6-BO	17.23	
	PM6-B20:Y6-BO	16.06	
ITO/ZnO/ Active layer /MoO_3/Al	PTQ10:Y6	14.2	[27]
	PTQ10:Y6(LBL)	14.4	
	PTQ10:Y6(LBL+Anneal)	14.5	
	PTQ10:Y6(LBL+Anneal+DIO)	13.7	

ITO/2PACz/ Active layer /PNDIT-F3N/Ag	D18:L8-BO:PY-C11	17.83	[28]
	D18:L8-BO:PY-C11+HBT-1	18.76	
ITO/PEDOT:PSS/Active layer/PDINN/Ag	PM6:L8-BO:5%SBS	17.21	[29]
	PM6:L8-BO:10%SBS	16.28	
	PM6:L8-BO	18.17	
ITO/2PACz/ Active layer /PDINN/Ag	PM6-H:BTP-eC9	18.15	[18]
	PM6-OH:BTP-eC9	18.50	
	PM6-UR:BTP-eC9	17.97	
ITO/PEDOT: PSS /Active layer/ PNDIT-F3N/Ag	PNTB6-Cl:BTP-Si4	16.4	[15]
	PNTB6-Cl:BTP-Si4:Y6	17.0	
ITO/2PACz/ Active layer /PDINN/Ag	**PM6:BTP-eC9**	**18.04**	**This work**
	PM6:BTP-eC9:5% PP-Cl	**18.69**	
	D18:BTP-eC9:L8-BO	**19.85**	
	D18:BTP-eC9:L8-BO:PP-Cl	**20.50**	

Table S11. Photovoltaic performance of D18:BTP-eC9:L8-BO:5% PP-Cl based *IS-OPVs* under the optimized conditions [a)].

Active layer	V_{OC}**(V)**	J_{SC} **(mA/cm^2)**	**FF (%)**	**PCE (%)**
D18:BTP-eC9:L8-BO	0.826	27.53	69.50	15.81 (15.76±0.04)
D18:BTP-eC9:L8-BO: PP-Cl	0.829	27.44	70.73	16.10 (15.97±0.09)

[a)] All the detailed PCE data were obtained by averaging the data of the 6 samples.

Table S12. PCE $_{\text{max}}$ and S_{80} of the *IS-OPVs* reported in the literature and in this work.

Year	Active layer	PCE $_{\text{max}}$ (%)	S_{80} (%)	Ref
2016	P3HT: PCBM	1.25	7.0	[30]
2017	PTB7-Th: PC71BM	6	8.1	[31]
2019	PTzNTz: $PC_{71}BM$	9.7	7.7	[32]
2021	PBDB-T: PCE10: N2200	6.33	11.2	[33]
2021	PM6 : $PC_{71}BM$	5.7	5.1	[34]
2022	PM6: Y7: PVH (N2200 40%)	9.03	28	[35]
	PM6: Y7: N2200	11.71	20	
2022	PBDB-T: PYFS-Reg	10.64	22.4	[36]
2022	PM6-OEG5: BTP-eC9	11.78	20	[37]
2022	PM6: Y6-BO: N2200	10.2	34	[38]
2023	PM7-Thy10: L8-BO	13.69	43	[39]
2023	PETTCVT-H: L8-BO	10.1	16	[40]
2023	PM6-b-PDMS: L8-BO	11.34	36	[41]
2023	PM6-OEG5: BTP-eC9: P(NDI2OD-TCVT	12.18	32	[42]
2023	PBQx-TF: P1, P2: PYIT	13.7	35	[43]
2023	PM6: Y6-BO: N2200	13.1	34	[44]
2024	PM6: Y6: BAC	12.8	20	[45]

2024	PM6: PM6-HD: BTP-eC9	13.82	21	46
2024	PM6: N3: SEBS	9.4	20	47
2024	D18$_{0.4}$: SEBS$_{0.6}$/L8-BO	12.13	50	8
2024	PM6-OEG5: Y6-BO: N2200	11.26	20	48
2024	PBQx-TCl: PYF-IT: N2200	12.6	51	11
2025	PNTB6-Cl:BTP-Si4:	14.6	80	15
2025	PM6: BTP-eC9: TDY-α	15.1	9	49
2025	PM6: PY-DT	16.74	75	50
2025	PM6: IDTBT: PY-IT	14.2	30	51
2026	PM6: PYF-T-*o*: SEBS	14.07	30	22
2026	PM6: BTP-eC9	14.0	10	52
	PM6: PY-IT	13.4	15	
2026	**PM6: BTP-eC9**	**15.02**	**8.4**	**This work**
	PM6: BTP-eC9: PP-Cl	**15.54**	**28.4**	
	D18: BTP-eC9:L8-BO	**15.81**	**9.8**	
	D18: BTP-eC9:L8-BO: PP-Cl	**16.10**	**31.6**	

[a] The S_{80} is defined as the strain at 80% of the initial PCE.

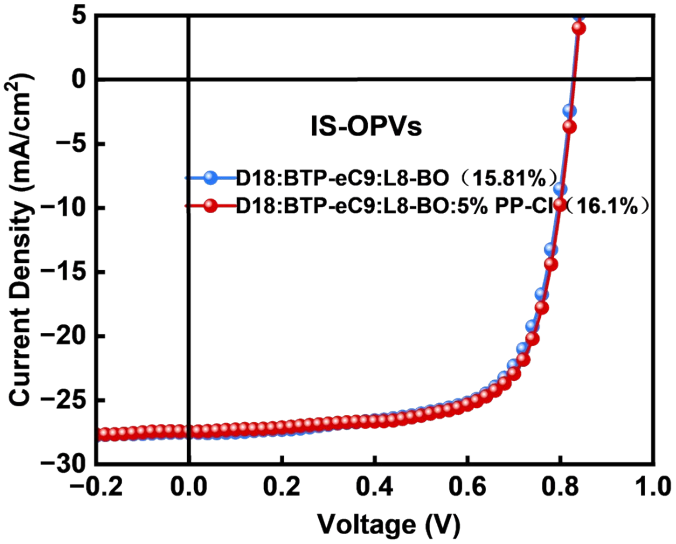

Figure S12. *J-V* curves of rigid D18:BTP-eC9:L8-BO ternary devices with and without 5 wt% PP-Cl.

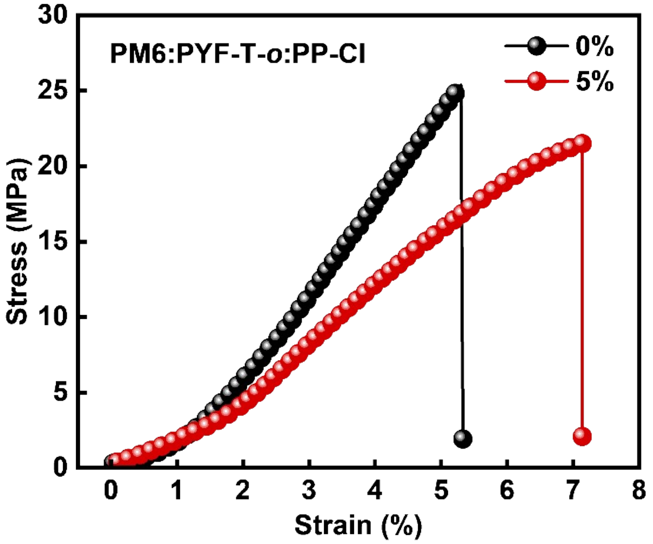

Figure S13 Stress-strain curves of the PM6:PYF-T-*o* blend films with 5%wt PP-Cl contents.

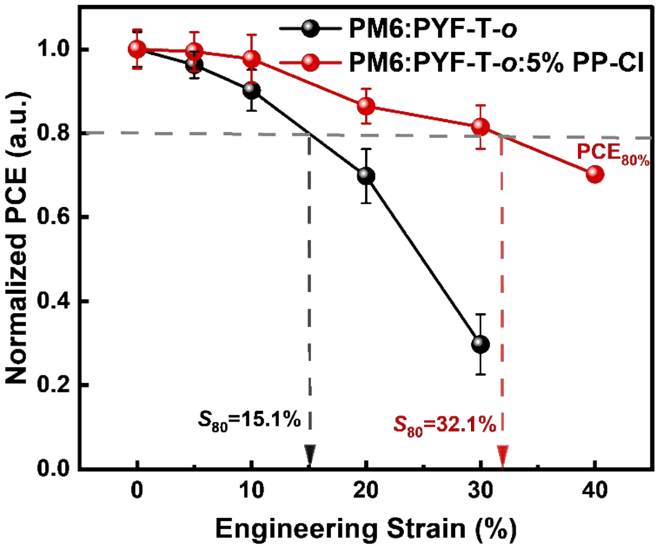

Figure S14 Normalized PCE of the devices of PM6: PYF-T-*o*:5%PP-Cl based *IS*-*OPVs*.

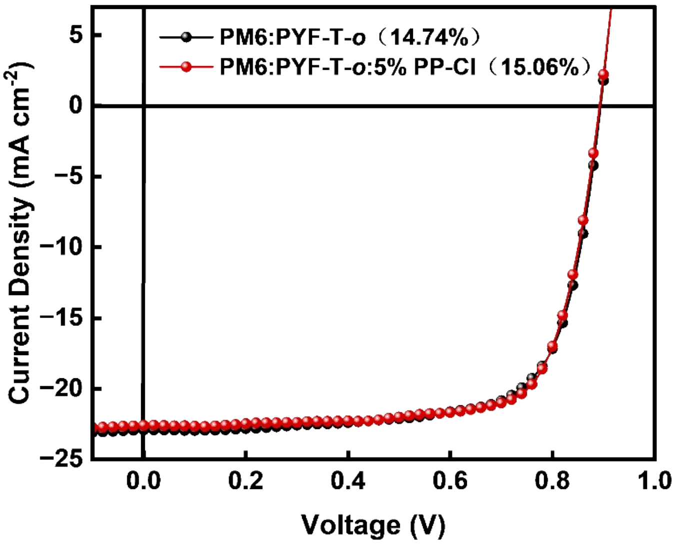

Figure S15**.** *J-V* curves of the PM6: PYF-T-*o* stretchable devices with and without 5 wt% PP-Cl

Table S13**.** Photovoltaic performance of *IS-OPVs* under the optimized conditions.[a)]

Active layer	V_{OC}(V)	J_{SC} (mA/cm^2)	FF (%)	PCE (%)
PM6: PYF-T-*o*	0.894	22.90	71.99	14.74 (14.55±0.13)
PM6: PYF-T-*o*: 5%PP-Cl	0.892	22.57	74.80	15.06 (14.94±0.08)

[a)] All the detailed PCE data were obtained by averaging the data of the 6 samples.

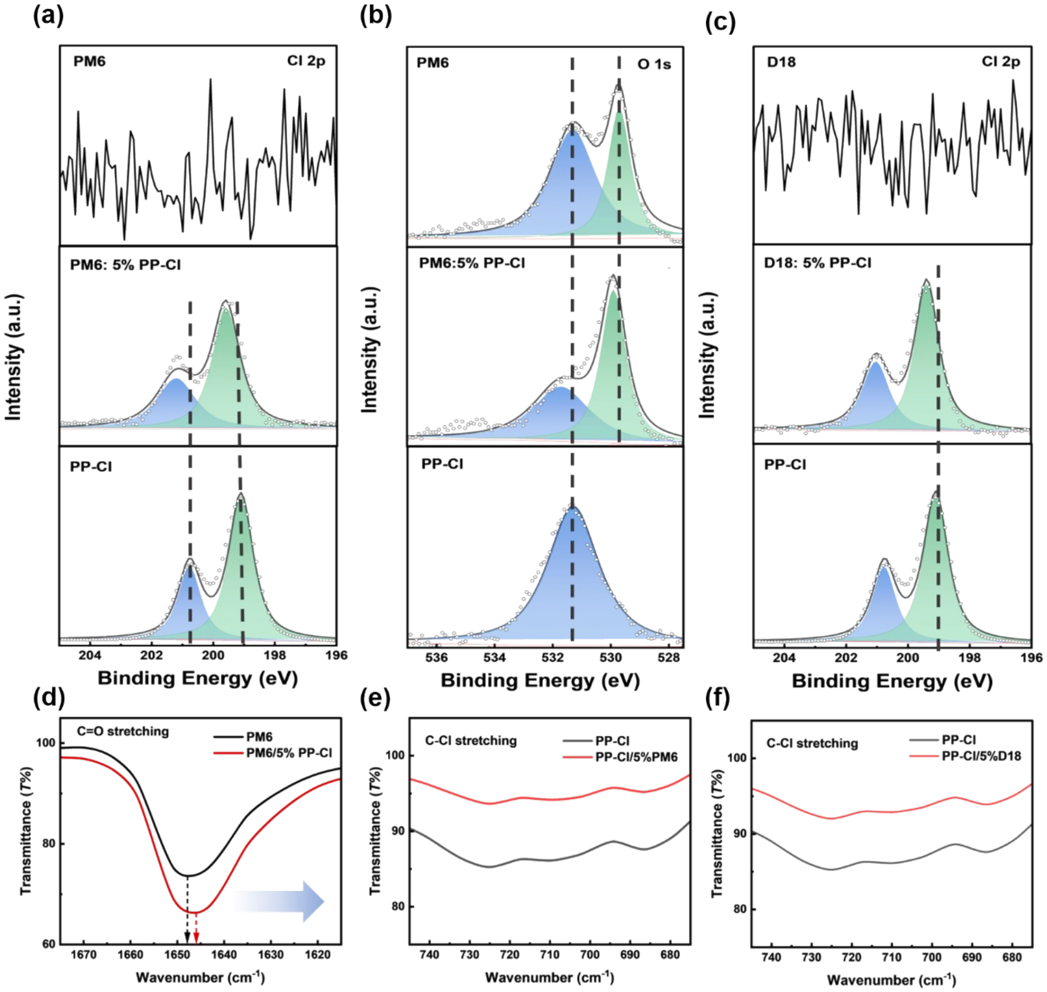

Figure S16. (a) Cl 2p and (b) O 1s XPS spectra of PM6, PP-Cl and PM6/ 5% PP-Cl. (c) Cl 2p XPS spectra of D18, PP-Cl and D18/ 5% PP-Cl. (d) FT-IR spectra of PM6 and PM6/5% PP-Cl for C=O bonds. (e) FT-IR spectra of PP-Cl, and PP-Cl/5% PM6 for C-Cl bonds. (f) FT-IR spectra of PP-Cl, and PP-Cl/5% D18 for C-Cl bonds.

From a mechanical standpoint, the toughening effect at low PP-Cl loading appears to arise from a combination of interfacial stress dissipation and preservation of the semiconducting network. The ordered semiconducting domains retain the mechanical strength and transport functionality of the host blend, whereas the more compliant PP-Clrich regions provide additional deformability and promote more uniform stress redistribution. In this context, chlorine-involved reversible weak interactions and chain entanglement likely contribute sacrificial energy-dissipation pathways during deformation, thereby delaying crack initiation and increasing both elongation at break and toughness. Li *et al.*[53] previously proposed that "CH_2-CHCl" in PVC could interact with donor materials (*e.g.*, PM6) containing carbonyl units to form a "cyclohexyl-like" structure. In order to verify whether PP-Cl has a similar effect as PVC, we utilized X-ray photoelectron spectroscopy (XPS) to probe the intermolecular forces between PM6 and PP-Cl, as presented in **Figure S16**a, b. The Cl 2p XPS spectra showed no detectable signal for neat PM6 (consistent with its chlorine-free composition), while pure PP-Cl exhibited a characteristic doublet at 200.7 eV (Cl $2p_{3/2}$) and 199.1 eV (Cl $2p_{1/2}$). In the PM6/PP-Cl composite film, this doublet appeared at 201.2 eV and 199.5 eV **(Figure S16**a**)**, exhibiting a positive binding energy shift that indicates reduced electron density on the chlorine centers. In parallel, the O 1s XPS spectra of PM6/PP-Cl blends displayed measurable shifts relative to pristine PM6 films: the 529.7 eV peak observed in both neat PM6 and the composite shifted to 529.9 eV in the blended film **(Figure S16**b**)**, signifying decreased electron density on PM6's oxygen atoms. Taken together, these consistent binding energy shifts confirm the formation of noncovalent interactions between the chlorine atoms of PP-Cl and the oxygen atoms of PM6.

To consolidate such intermolecular interaction evidence, we further supplemented the XPS results with Fourier transform infrared spectroscopy (FT-IR) measurements **(Figure**

S16d, e**)**. The characteristic peak centered at ~1650 cm^{-1} for pristine PM6 originates from the stretching vibration of C=O carbonyl groups; upon blending with 5 wt% PP-Cl, this carbonyl peak displays an obvious red shift toward lower wavenumber **(Figure S16**d**)**. In the pure PP-Cl spectrum, the dual absorption valleys located at ~690 cm^{-1} and ~720 cm^{-1} are assigned to aliphatic C–Cl stretching vibrations, and these paired C-Cl characteristic peaks show evidently reduced absorption intensity after doping with 5 wt% PM6**(Figure S16**e**)**. The redshift of PM6 carbonyl together with the weakened C-Cl absorbance of PP-Cl in binary blends jointly verifies the formation of noncovalent intermolecular interactions between the carbonyl moieties on PM6 backbones and the C-Cl functional groups of PP-Cl chains. Collectively, these FT-IR variations confirm the existence of weak intermolecular contact between PM6 and PP-Cl, analogous to the interaction behavior between carbonyl-containing donor polymers and PVC, which enables effective stress dissipation without irreversibly destroying the intrinsic D-A conjugated skeleton of the active layer.

Notably, this halogen bond-dominated mechanism of multiple weak noncovalent interactions exhibits excellent universality and is equally applicable to the carbonyl-free D18 donor polymer system. Although D18 lacks the strong C=O acceptor sites present in PM6, the conjugated π-electrons, heterocyclic N atoms, side-chain F atoms, and aromatic C-H bonds on its backbone can all act as weak halogen bond acceptors to interact with the C-Cl bonds of PP-Cl. This is directly confirmed by the spectral changes in D18/PP-Cl blend films, where the characteristic C-Cl stretching vibration peaks of PP-Cl at ~690 cm^{-1} and

~720 cm^{-1} weaken significantly with increasing D18 doping concentration **(Figure S16**f**)**, a trend that is identical to that observed in the PM6/PP-Cl system. It should be noted that although the fundamental working mechanism of PP-Cl is identical in both systems, the magnitude of photovoltaic performance improvement differs between them. This discrepancy does not arise from divergent working mechanisms but rather likely stems from the inherent morphological differences between the two pristine blend films: the PM6:BTP-eC9 binary film has already achieved optimal phase separation and molecular packing in its pristine state, so PP-Cl mainly enhances the fill factor by passivating interfacial traps and suppressing charge recombination; in contrast, the pristine D18:BTP-eC9:L8-BO ternary film exhibits relatively poor phase separation, and PP-Cl can further optimize the phase morphology and molecular arrangement by modulating interfacial tension, thereby simultaneously improving both the short-circuit current density and fill factor. We have also added the experimental data of XPS. The data clearly indicates that there is indeed a weak interaction between D18 and PP-Cl **(Figure S16**c**)**.

References

1. Y. Yan, B. Duan, M. Ru, Q. Gu, S. Li and W. Zhao, Advanced Energy Materials, 2025, **15**, 2404233.
2. Y. Bai, S. Li, Q. Wang, Q. Chen, Z. Zhang, S. Meng, Y. Zang, H. Fu, L. Xue, L. Ye and Z.-G. Zhang, National Science Review, 2025, **12**.
3. X. Luo, X. Liu, Y. Lin, M. Li, Z. Yang, Z. Xiong, Y. Wang, F. Peng, W. Zhong, N. Li and L. Ying, Angewandte Chemie International Edition, 2025, **64**, e202514985.
4. H. Chen, K. Sun, Z. Wei, S. Liu, Z. Xia, J. Shuai, Z. Wang, W. Chen, J. Wei, K. Chen, Z. Zhou, Y. Sun, P. You, H. Hu, G. Zhang and F. Yan, Advanced Functional Materials, 2026, https://doi.org/10.1002/adfm.202528623.
5. Y. Liang, D. Zhang, Z. Wu, T. Jia, L. Lüer, H. Tang, L. Hong, J. Zhang, K. Zhang, C. J. Brabec, N. Li and F. Huang, Nature Energy, 2022, **7**, 1180-1190.
6. G. Wang, Y. Cui, M. Ou, Y. Yu, Y. Xiao, H. Yuan, T. Zhang, Z. Chen, N. Yang, L. Ma, R. Yu, S. Zhang and J. Hou, Joule, 2026, **10**, 102263.
7. B. Shi, Y. Li, J. Sun, R. Sun, D. Jiang, R. Zhou, R. Zhang, J. Qiao, S. H. Pun, J. Yi, X. Xia, P. Lu, Y. Wang, G. Zhang, T. He, M. Zhang, Z. Ji, X. Du, J. Min, F. Chen, F. Gao, X. Hao, H. Yan and H. Yin, Advanced Materials, 2025, **37**, e05313.
8. J.-W. Lee, T. H.-Q. Nguyen, E. S. Oh, S. Lee, J. Choi, H. S. Kwon, C. Wang, S. Lee, J.-Y. Lee, T.-S. Kim and B. J. Kim, Advanced Energy Materials, 2024, **14**, 2401191.
9. A. Wupur, T. Chen, J. Yu, S. Su, X. Wu, Y. Li, Y. Zhu, J. Dong, Y. Yang, B. Zhang, L. Zhan, J. Wu, Z. Ma, Y. Li, W. Fu and H. Chen, Advanced Materials, 2026, **38**, e14741.
10. P. Wang, F. Bi, Y. Li, C. Han, N. Zheng, S. Zhang, J. Wang, Y. Wu and X. Bao, Advanced Functional Materials, 2022, **32**, 2200166.
11. D. Han, K. Zhou, X. Li, P. Lv, J. Wu, H. Ke, W. Zhao and L. Ye, Advanced Functional Materials, 2024, **34**, 2407392.
12. S. Li, Y. Yang, Y. Bae, Y. Li, H. Y. Woo, Y. Geng and L. Ye, Advanced Energy Materials, 2025, https://doi.org/10.1002/aenm.202506761.
13. C. Sun, S. Li, V. Kuvondikov, S. Nematov and L. Ye, Science China Materials, 2025, **68**, 3042-3059.
14. H. Ke, H. Xie, L. Pei, M. Gao, S. Li, D. Sheng, D. Urazkulova, V. Kuvondikov, S. Nematov, X. Li and L. Ye, Chinese Journal of Chemistry, 2025, **43**, 2909-2916.
15. Z. Wang, D. Zhang, L. Yang, O. Allam, Y. Gao, Y. Su, M. Xu, S. Mo, Q. Wu, Z. Wang, J. Liu, J. He, R. Li, X. Jia, Z. Li, L. Yang, M. D. Weber, Y. Yu, X. Zhang, T. J. Marks, N. Stingelin, J. Kacher, S. S. Jang, A. Facchetti and M. Shao, Science, 2025, **387**, 381-387.
16. R. Zeng, L. Zhu, M. Zhang, W. Zhong, G. Zhou, J. Zhuang, T. Hao, Z. Zhou, L. Zhou, N. Hartmann, X. Xue, H. Jing, F. Han, Y. Bai, H. Wu, Z. Tang, Y. Zou, H. Zhu, C.-C. Chen, Y. Zhang and F. Liu, Nature Communications, 2023, **14**, 4148.

17. H. Wang, C. Xiao, H. Geng, Y. Liu, J. Xu, Z. Lu, H. Fan, Y. Zhen and W. Li, Macromolecules, 2025, **58**, 9809-9818.
18. Z. Gao, Q. Chen, M. Duan, Z. Lu, J. Wu, C. Xiao, C. R. McNeill and W. Li, Angewandte Chemie International Edition, 2026, **65**, e24211.
19. S. Li, Y. Wang, C. Sun, J. Feng, J. Zuo, B. Sun, D. Han, M. Gao, X. Li, B. Xiao, W. Zhao, V. Kuvondikov, S. Nematov, T. Jia, G. Zhang and L. Ye, Advanced Materials, 2026, **38**, e16229.
20. J. Feng, S. Li, C. Sun, J. Wu and L. Ye, Macromolecules, 2025, **58**, 6667-6677.
21. Z. Peng, K. Xian, Y. Cui, Q. Qi, J. Liu, Y. Xu, Y. Chai, C. Yang, J. Hou, Y. Geng and L. Ye, Advanced Materials, 2021, **33**, 2106732.
22. B. Sun, X. Li, W. Zhao, K. Zhang, S. Li, C. Sun, V. Kuvondikov, S. Nematov, M. Lv and L. Ye, Advanced Functional Materials, 2026, **36**, e12584.
23. C. Sun, S. Li, J. Feng, W. Zhao, Y. Chen, M. Gao, V. Kuvondikov, S. Nematov and L. Ye, Advanced Materials, 2026, **38**, e20990.
24. F. Arshad, M. Haris, E. S. Oh, Z. Ullah, D. H. Ryu, S. Lee, H. K. Lee, S. K. Lee, T.-S. Kim, H.-W. Kwon, C. E. Song and W. S. Shin, Advanced Functional Materials, 2024, **34**, 2402045.
25. J. Zhu, Q. Kang, Y. Zang, K. Yuan, Z. Chen, Y. Wang, J. Wang and J. Hou, Advanced Functional Materials, 2026, e25182.
26. J. Kim, G.-U. Kim, D. J. Kim, S. Lee, D. Jeong, S. Seo, S.-J. Ko, S. C. Yoon, T.-S. Kim and B. J. Kim, Journal of Materials Chemistry A, 2023, **11**, 4808-4817.
27. Q. Zhu, J. Xue, G. Lu, B. Lin, H. B. Naveed, Z. Bi, G. Lu and W. Ma, Nano Energy, 2022, **97**, 107194.
28. S. Wang, S. Wang, J. Wang, N. Yu, J. Qiao, X. Xie, C. Li, M. S. Abbasi, R. Ding, X. Zhang, Y. Han, G. Lu, J. Zhang, X. Hao, Z. Tang, Y. Cai and H. Huang, Advanced Energy Materials, 2026, **16**, 2405205.
29. J. Zhang, Q. Chen, M. Li, G. Zhang, Z. Zhang, X. Deng, J. Xue, C. Zhao, C. Xiao, W. Ma and W. Li, Advanced Materials, 2024, **36**, 2312805.
30. E. J. Sawyer, A. V. Zaretski, A. D. Printz, N. V. de los Santos, A. Bautista-Gutierrez and D. J. Lipomi, Extreme Mechanics Letters, 2016, **8**, 78-87.
31. Y.-Y. Yu, C.-H. Chen, C.-C. Chueh, C.-Y. Chiang, J.-H. Hsieh, C.-P. Chen and W.-C. Chen, ACS Applied Materials & Interfaces, 2017, **9**, 27853-27862.
32. Z. Jiang, K. Fukuda, W. Huang, S. Park, R. Nur, M. O. G. Nayeem, K. Yu, D. Inoue, M. Saito, H. Kimura, T. Yokota, S. Umezu, D. Hashizume, I. Osaka, K. Takimiya and T. Someya, Advanced Functional Materials, 2019, **29**, 1808378.
33. Q. Zhu, J. Xue, L. Zhang, J. Wen, B. Lin, H. B. Naveed, Z. Bi, J. Xin, H. Zhao, C. Zhao, K. Zhou, S. Liu and W. Ma, Small, 2021, **17**, 2007011.
34. J. Noh, G.-U. Kim, S. Han, S. J. Oh, Y. Jeon, D. Jeong, S. W. Kim, T.-S. Kim, B. J. Kim and J.-Y. Lee, ACS Energy Letters, 2021, **6**, 2512-2518.
35. J.-W. Lee, G.-U. Kim, D. J. Kim, Y. Jeon, S. Li, T.-S. Kim, J.-Y. Lee and B. J. Kim, Advanced Energy Materials, 2022, **12**, 2200887.

36. J.-W. Lee, C. Sun, S.-W. Lee, G.-U. Kim, S. Li, C. Wang, T.-S. Kim, Y.-H. Kim and B. J. Kim, Energy & Environmental Science, 2022, **15**, 4672-4685.
37. J.-W. Lee, C. Lim, S.-W. Lee, Y. Jeon, S. Lee, T.-S. Kim, J.-Y. Lee and B. J. Kim, Advanced Energy Materials, 2022, **12**, 2202224.
38. Z. T. Gebremichael, C. Ugokwe, S. Alam, S. Stumpf, M. Diegel, U. S. Schubert and H. Hoppe, RSC Advances, 2022, **12**, 25593-25604.
39. Q. Wan, S. Seo, S.-W. Lee, J. Lee, H. Jeon, T.-S. Kim, B. J. Kim and B. C. Thompson, Journal of the American Chemical Society, 2023, **145**, 11914-11920.
40. J.-W. Lee, T. N.-L. Phan, E. S. Oh, H.-G. Lee, T.-S. Kim and B. J. Kim, Advanced Functional Materials, 2023, **33**, 2305851.
41. S. Seo, J.-W. Lee, D. J. Kim, D. Lee, T. N.-L. Phan, J. Park, Z. Tan, S. Cho, T.-S. Kim and B. J. Kim, Advanced Materials, 2023, **35**, 2300230.
42. C. Lim, S. Park, D. J. Kim, J.-W. Lee, J.-S. Park, S. Seo, D. Kim, F. S. Kim, T.-S. Kim and B. J. Kim, Journal of Materials Chemistry A, 2023, **11**, 20031-20042.
43. G.-U. Kim, C. Choi, D. Jeong, D. J. Kim, T. N.-L. Phan, S. Song, J. Park, T.-S. Kim, Y.-H. Kim and B. J. Kim, Advanced Energy Materials, 2023, **13**, 2302125.
44. J. Lee, J.-W. Lee, H. Song, M. Song, J. Park, G.-U. Kim, D. Jeong, T.-S. Kim and B. J. Kim, Journal of Materials Chemistry A, 2023, **11**, 12846-12855.
45. Z. Wang, D. Zhang, M. Xu, J. Liu, J. He, L. Yang, Z. Li, Y. Gao and M. Shao, Small, 2022, **18**, 2201589.
46. X. Li, H. Ke, S. Li, M. Gao, S. Li, J. Yu, H. Xie, K. Zhou, K. Zhang and L. Ye, Advanced Functional Materials, 2024, **34**, 2400702.
47. Z. Peng, S. Li, K. Zhou, Y. Zhang, M. Li, X. Li, C. Yang, F. Bian, Y. Geng and L. Ye, Advanced Energy Materials, 2024, **14**, 2304286.
48. Y. Liu, C. Xie, W. Lai, Z. Bu, G. Zhang, C. Xiao and W. Li, Advanced Materials Technologies, 2024, **9**, 2301321.
49. K. Xian, K. Zhang, T. Zhang, K. Zhou, Z. Zhang, J. Hou, H. Zhang, Y. Geng and L. Ye, Energy & Environmental Science, 2025, **18**, 2570-2583.
50. H. Li, S. Zeng, H. Zhao, Q. Liu, T. Xue, S. Liu, H. Li, L. Hu, E. Zhou, M. Khumalo, X. Hu and Y. Chen, Advanced Materials, 2025, **37**, 2507761.
51. L. Pei, D. Han, Y. Wang, M. Gao, J. Wu, C. Sun, M. Yu, Y.-X. Wang, H. Ke, X. Li and L. Ye, Advanced Functional Materials, 2025, **35**, 2425892.
52. Y. Bae, S. Li, W. Zhao, M. Tugolbay and L. Ye, Advanced Functional Materials, 2026, **36**, e74985.
53. C. Guan, C. Xiao, X. Liu, Z. Hu, R. Wang, C. Wang, C. Xie, Z. Cai and W. Li, Angewandte Chemie International Edition, 2023, **62**, e202312357.